Mitigating Radome Induced Bias in X-Band Weather Radar Polarimetric moments using Adaptive DFT Algorithm.

Thiruvengadam PADMANABHAN[1,2], Guillaume LESAGE[1], Ambinintsoa Volatiana RAMANAMAHEFA[1], and Joël VAN BAELEN[1]

[1]LACY, Université de La Réunion/CNRS/MétéoFrance, Saint-Denis, La Réunion.
[2]School of Meteorology, University of Oklahoma, Norman, Oklahoma, USA.

Correspondence to: Thiruvengadam PADMANABHAN (thiruvengadam7892@gmail.com) and Joël VAN BAELEN (joel.van-baelen@univ-reunion.fr)

Abstract. In recent years, the application of compact and cost-effective deployable X-band polarimetric radars has gained in popularity, particularly in regions with complex terrain. The deployable radars generally use a radome constructed by joining multiple panels using metallic threads to facilitate easy transportation. As a part of the ESPOIRS project, Laboratoire de l'Atmosphère et des Cyclones has acquired an X-band meteorological radar with four panel radome configuration. In this study, we investigated the effect of the radome on the measured polarimetric variables, particularly differential reflectivity and differential phase. Our observations reveal that the metallic threads connecting the radome panels introduce power loss at vertical polarization, leading to a positive bias in the differential reflectivity values. To address the spatial variability bias observed in differential reflectivity and differential phase, we have developed a novel algorithm based on the Discrete Fourier Transform. The algorithm's performance was tested during an intense heavy rainfall event caused by the Batsirai cyclone on Reunion Island. The comparative and joint histogram analysis demonstrates the algorithm's effectiveness in correcting the spatial bias in the polarimetric variables.

Keywords: Radome joints, Spatial bias, X-band Weather radar, ZDR, PHIDP, Adaptive DFT algorithm, Polarimetric variables, Batsirai cyclone, Multi-panel radome.

1. INTRODUCTION

Doppler weather radars provide comprehensive precipitation measurements at high spatial resolution, offering valuable insights into the orography-influenced precipitation processes (Georgis et al., 2000). Among different frequency bands, X-band radars have gained popularity due to their compact size and affordable cost, making them well-suited for deployment in areas with challenging topography. Additionally, modern polarimetric technology has dramatically enhanced the ability of X-band radars to estimate precipitation, overcoming their traditional limitation of high attenuation rates in the rain (Ryzhkov et al., 1994). The ESPOIRS (Etude des Systèmes Précipitants de l'Océan Indien par Radars et Satellites) project implemented by LACy (Laboratoire de l'Atmosphère et des Cyclones) has utilized the advantages of X-band polarimetric radar to examine the dynamics and variability of intense tropical precipitation at the local scale, particularly its interaction with the relief of the island. Initially, an X-band radar operating at 9.41 GHz was deployed south of Reunion Island (Figure 1a) to investigate heavy rainfall and the pronounced relief effects that may contribute to rainfall intensification. Later, the radar was installed in Seychelles and Madagascar to explore different geographical and meteorological contexts. The radar used for this study is a GAMIC GMWR-25-DP, which by design

37 has the transceiver unit fixed just behind the antenna so that the transceiver and the antenna move together and avoid the use of

38 rotary joints.

39 Although X-band polarimetric radar offers advantages over single polarization radars, maintaining the accuracy of its polarimetric

40 data requires rigorous quality control (Park et al., 2005). One factor that can impact the performance of the radars is the radome.

41 While they play a protective role, radome can passively affect the observations due to material-related transmission losses and

42 variations in sidelobe levels (Figueras i Ventura et al., 2021; Mishra et al., 2014). Mainly, radome panels with metallic threads at

43 their joints, common in mobile radars, can introduce biases in polarimetric observations (Figueras i Ventura et al., 2021; Gourley

44 et al., 2006). The ESPOIRS X-band radar is protected by a composite radome with a 1.435m base diameter and 2m height,

45 consisting of four fiberglass-reinforced lateral segments attached through horizontally aligned metal nuts and bolts arranged along

46 the vertical axis (Figure 1b, 1c). Radar data from the Batsirai cyclone on 3 February2022 show significant biases in differential

47 reflectivity (ZDR) and differential phase (PHIDP). One of the objectives of this study is to identify the source of these biases and

48 hypothesize that they originate from the radome metal joints.

49 In similar scenarios, efforts have been made to address biases using spatial calibration curves from radar data (Figueras i Ventura

50 et al., 2021; Gourley et al., 2006). However, the stochastic nature of radar measurements introduces inherent uncertainty into

51 calibration curves, leading to an overall increase in measurement uncertainty. Previous investigations have also recommended the

52 implementation of a seamless monoblock radome to mitigate spatial bias, as it eliminates the presence of joints and, subsequently,

53 any bias. Nevertheless, the unique design of the portable ESPOIRS X-band radar, which prioritizes ease of transportation, presents

54 inherent challenges in adopting a monoblock radome solution. To address this challenge, this study proposes an adaptive Discrete

55 Fourier Transform (DFT) based algorithm to mitigate the bias. This algorithm effectively utilizes the information available in radar

56 scans and enables the correction of the ZDR and PHIDP moments for various scan strategies.

57 The distinguishing feature of this algorithm is its capacity for dynamic threshold adjustment in the correction of frequency values

58 generated by the DFT based on the characteristics of radar moments. Such adaptivity sets this algorithm apart from traditional

59 methods (Figueras i Ventura et al., 2021; Gourley et al., 2006), which employ fixed spatial calibration curves. To assess the

60 performance of the proposed algorithm, it is applied to correct the ZDR and PHIDP radar scans obtained during an intense heavy

61 rainfall event caused by the passage of the Batsirai cyclone in the vicinity of Reunion Island on February 2 to 4, 2022. The proposed

62 method is designed to correct spatial biases in ZDR and PHIDP measurements, not absolute biases that are constant across all

63 azimuth directions and elevations. Correcting absolute biases that are uniform across all measurements was not the intent of our

64 study. Section II focuses on the source of the spatial bias in ZDR, offering insights into the factor responsible for this bias. The

65 adaptive DFT algorithm proposed in this study is introduced in section III, providing a discussion of its mathematical formulation.

66 Section IV assesses the proposed algorithm's performance through comparative and joint histogram analysis. Section V

67 summarizes the key points of the study and outlines the direction of future research to test further and enhance the algorithm's

68 performance.

69 **2.   SOURCE OF BIAS**

70 To elucidate the origins of positive bias in PHIDP measurements and ascertain its underlying causes, this study employs a

71 comprehensive approach involving the calculation of PHIDP offsets for all PPI scans conducted on the 2/3/2022 case study,

72 following the technique outlined in previous works (Figueras i Ventura et al., 2012), which utilized PHIDP offsets to discern the

73   influence of radome joints. The findings in Figure 1d exhibit a box plot distribution of PHIDP offsets across various azimuth

74   angles. Figure 1d shows a sinusoidal azimuthal pattern with four periods in the PHIDP offset. Strikingly, a distinct correlation

75   emerges between the azimuthal period positions of the PHIDP offsets and the orientation of the radome joints, with notable

76   alignment occurring at approximately ~~35~~55, 85, 175 and 265 degrees. This observation strongly suggests that the metallic threads

77   and joint configuration are the key factors contributing to the bias in PHIDP. The localization of the bias near the joints is due to

78   signal phase sensitivity to path length and material properties. Radome metal joints can introduce significant phase shifts in specific

79   polarizations, impacting PHIDP measurements when signal paths intersect with these joints (Li et al., 2017), explaining the

80   observed PHIDP offset collocation with the radome joint direction.

81   The positive bias observed in ZDR ~~(Figure 2a)~~ can result from either an increase in horizontal reflectivity values (ZH) or a decrease

82   in vertical reflectivity values (ZV). To ascertain the cause of the positive bias in ZDR, the temporal median of horizontal and

83   vertical reflectivity obtained from RHI scan angles of 28, 300, 45 and 76 degrees on 3rd February 2022 were computed. _These_

84   _specific azimuth angles were selected as they were the only available RHI scans for analysis._ Subsequently, for each median RHI

85   scan at 28, 300, 45 and 76 degrees of azimuth respectively, elevation angles exhibiting positive ZDR bias (70, 70, 36, and 34) and

86   unbiased elevation angles (66, 67, 31, and 27) were identified for both horizontal and vertical polarization and compared as shown

87   in Figure 2a-2d. The biased (red, blue) and unbiased (black, green) elevation angles were chosen sufficiently close to each other

88   to ensure that the same hydrometeor characteristics were observed. _For example, the 34° angle marks the transition where the onset_

89   _of radome-induced bias becomes visible and was chosen as it is the closest elevation angle to 27° (unbiased) that still observes the_

90   _same precipitation pattern._

91   Figures 2a and 2b show that the horizontal reflectivity values in biased and unbiased elevation angles (red, black) exhibit a

92   consistent covariation pattern with a negligible offset. Consequently, one would expect the vertical reflectivity values (blue, green)

93   to follow a similar trend. However, it is observed that the vertical reflectivity values correlate with each other but with an offset.

94   Specifically, the biased elevation angle's vertical reflectivity (blue) has a negative offset compared to the unbiased elevation angle's

95   vertical reflectivity (green). At lower elevation angles of RHI scans, where the variance of reflectivity values across the range

96   direction is limited, a noticeable decrease in vertical reflectivity in the biased region is prominent. Specifically, at lower elevation

97   angles of the RHI scans at 45 and 76 degrees of azimuth (Figure 2c and 2d), the vertical reflectivity values in the biased region are

98   noticeably lower than their corresponding horizontal and vertical reflectivity values in the unbiased region. This indicates that the

99   metal joints have exerted a notable influence on the propagation of microwaves, particularly regarding vertical polarization. This

100   influence has led to a systematic bias in ZDR.

101   From Figures 4a and 4c, it can be noted that PHIDP and ZDR exhibit biases at somewhat different azimuth angle locations. The

102   observed bias in ZDR at varying angles, compared to the bias in PHIDP, can be attributed to distinct scattering characteristics. The

103   ZDR's azimuthal bias could arise from factors related to the scattering of incident power from the main lobe around the metallic

104   threads, which could potentially amplify the impact of the side lobes. These increased side lobe levels cause more energy to be

105   radiated or received in undesirable directions, potentially amplifying susceptibility to noise or interference from those directions

106   (Frech et al., 2013). This differs from PHIDP's bias, which is primarily influenced by the path length the radar signals traverse (Li

107   et al., 2017). Hence, the PHIDP bias are observed in the direction of the radome joints. Detailed simulations or measurements are

108   imperative for a comprehensive understanding of the precise impact of radome joints on side lobe levels, phase delays, and their

109   correlation with ZDR and PHIDP.

110   3.   ADAPTIVE DFT ALGORITHM

111   This study introduces a DFT algorithm to mitigate the spatial bias present in the polarimetric variables. The correction procedure

112   starts by performing a Discrete Fourier transform on a single radar scan, which, in this case, corresponds to the 76° azimuth RHI

113   scan measured on 02/03/2022 01:08 UTC (Figure 3a). A one-dimensional DFT is applied along the range direction to the first 100

114   radar gates containing rain near the radar in order to process ~~to process~~ the polarimetric variable x for a particular azimuth or

115   elevation angle θ and N total range gates, as shown in equation 1, where n and k represent the range gate and frequency index,

116   respectively~~.~~. The transformation F[k] is repeated for each angle θ, respectively azimuth for PPI scans and elevation for RHI scans,

117   systematically covering the entire radar scan to obtain F[θ, k].

118   Subsequently, the power spectrum (P[θ, k]) is calculated from the obtained Fourier transform (F[θ, k]) for each azimuth/elevation

119   angle, as depicted in Figure 3c. In Figure 3c, a three-dimensional representation is shown, illustrating the power spectrum obtained

120   from the DFT for each elevation angle of the RHI scan. Notably, the power value of the zero frequency component (P[θ, 0]) derived

121   from various elevation angles, representing the DFT's DC component, reveals three distinct peaks corresponding to the spatial bias

122   pattern observed in Figure 3a's RHI scan. This indicates that a bias caused by the radome joints will result in a constant positive

123   increase of the magnitude all along the range, an offset, which will show up as an increase in the power value of the DC component

124   of the DFT spectrum.

125

126   $$F[\theta,k] = \sum_{n=0}^{N-1} e^{-2\pi j \frac{kn}{N}} x[\theta,n] \quad \text{for} \;\; 0 \le k < N \qquad (\text{-}1\text{-})$$

127

128   To address this bias, a correction factor (A/B) is introduced to filter the three peaks (Figure 3d) associated with the spatial bias.

129   Notably, the correction factor is only applied to the DC component values (F[θ, 0]) that exceed a certain adaptive threshold.

130

131   $$F[\theta,0]' = \begin{cases} F[\theta,0] \times \frac{A}{B} & \text{if } P[\theta,0] > \text{Median}(P[\theta,0]) \\ F[\theta,0] & \text{otherwise} \end{cases} \qquad (\text{-}2\text{-})$$

132

133   For all other frequency components k≠ 0, the values remain unchanged:

134

135   $$F[\theta,k]' = F[\theta,k] \;\; for\; k \neq 0 \qquad\qquad (3)$$

136

137   The threshold value is determined based on the moving median window of the power spectrum at the zeroth frequency

138   (Median(P[θ, 0]). For PPI scans, the moving median window encompasses all azimuth angles, covering a full 360 degrees. In

139   the case of RHI scans, the window includes all available 88 elevation angles. This approach simplifies implementation by

140   eliminating the need to define specific window sizes, which could vary with different scans or atmospheric conditions. The

141   correction factor is calculated as the ratio between the median values of F[θ, 0] corresponding to the power values below the

142   threshold (A) and the median values of F[θ, 0] corresponding to the power values above the threshold (B).

143

144   $$A = \text{Median}(F[\theta,0]) | P[\theta,0] < \text{Median}(P[\theta,0]) \qquad (\text{-}3\,4)$$

145   $$B = \text{Median}(F[\theta,0]) | P[\theta,0] > \text{Median}(P[\theta,0]) \qquad (\text{-}5\,4\text{-})$$

146   $$P[\theta,0] = \left[\sqrt{\text{Real}(F[\theta,0])^2 + \text{Img}(F[\theta,0])^2}\right]^2 \qquad (\text{-}6\,5\text{-})$$

147

148 Consequently, the zeroth frequency values that surpass the threshold are multiplied by the calculated correction factor, while the

149 remaining values are left uncorrected. Figure 3d shows the power $P[\theta, 0]$ from the DC component is characterized by distinct peaks

150 alongside the depiction of the adaptive threshold values and the reduced power after applying the correction factor. To derive the

151 corrected ZDR image (Figure 3b), an inverse Fourier transform is performed on all frequencies, encompassing the corrected DC

152 component.

153

154
$$x[\theta, k]' \; \cancel{x[\theta, n]} = \frac{1}{N} \sum_{k=0}^{N-1} e^{-2\pi j \frac{kn}{N}} \; F\cancel{F}[\theta, k]' \; \cancel{[\theta, k]} \qquad\qquad (\text{-}7\cancel{6}\text{-})$$

155

156 **4.   ASSESSMENT OF ADAPTIVE DFT FILTERING ALGORITHM EFFICIENCY**

157 The performance of the adaptive DFT filtering algorithm is assessed across different scan strategies (PPI and RHI) and different

158 polarimetric moments (ZDR and PHIDP) to determine its effectiveness. Figures 3a and 4a show increased spatial variability of

159 ZDR at specific azimuth and elevation angles of RHI and PPI scans, respectively, with a maximum variability of around 1.5-2 dB

160 observed. Similarly, Figures 4c and 5a depict increased spatial variability of PHIDP in PPI and RHI scans, with a magnitude of

161 variability around 8 to10 degrees. The application of the algorithm led to a substantial reduction in variability, as shown in Figures

162 3b, 4b, 4d and 5b. The proposed algorithm reduced the spurious ZDR variability from 1.5-2 dB to 1-1.34 dB, and the PHIDP

163 variability was reduced to less than 5 degrees. The results indicate the algorithm's effectiveness in mitigating spatial variability in

164 both ZDR and PHIDP values across all elevation angles and scanning strategies.

165   The relationship between ZDR and ZH provides insights into how raindrops deviate from a perfect spherical shape. Larger

166 raindrops exhibit higher horizontal reflectivity and have their long axis oriented in the horizontal direction compared to the vertical

167 direction, thereby showing signatures of higher ZDR values. Conversely, for lower values of horizontal reflectivity (less than 30

168 dBZ), we generally expect a ZDR value of nearly zero dB due to the near spherical shape of small drops. Therefore, comparing

169 the relationship between ZH and ZDR before and after applying the algorithm (Figure 6) shows how the correction has brought

170 the biased ZDR close to the expected value. Figures 6a and 6b show the joint histogram of ZDR and ZH for all the PPI scans

171 conducted on 3 February 2022 before and after applying the correction algorithm, with the marginal distribution of ZH in the top

172 and the marginal distribution of ZDR on the right side. Likewise, figures 6c and 6d show the joint histogram of ZDR and ZH for

173 all the RHI scans on the same date, before and after applying the correction algorithm. Figures 6a and 6b encompass data from all

174 PPI scans covering various azimuth angles and distances, whereas Figures 6c and 6d are specific to the RHIs for the four azimuth

175 angles chosen in Figure 2. This distinction accounts for the differences between Figures 6a and 6c (and likewise, Figures 6b and

176 6d). As these figures capture the data before any attenuation correction, the reflectivity distribution ranges from light drizzle (near

177 zero dBZ) to heavy rainfall ($\cong$40 dBZ). It can be observed from Figure 6a, 6c that the distribution of ZDR extends significantly

178 beyond 2dB for reflectivity values below 30 dBZ. Such increases arise from the spatial positive bias in ZDR discussed in view of

179 Figures 3a and 4a. The impact of the developed algorithm on the distribution of ZDR is highlighted in Figures 6b and 6d. Following

180 the correction, the mean distribution of ZDR shifts towards values closer to zero, approaching the theoretical values at lower

181 reflectivity. Furthermore, the correction also results in a noticeable increase in negative values of ZDR, indicating the presence of

182 differential attenuation fingerprints, a common occurrence in X-band radar systems, which were not as discernible before the

183 correction. Figures 6b and 6d reveal the impact of the algorithm in successfully addressing the positive bias in ZDR.

5.   CONCLUSION

This study investigates the impact of radome joints on the polarimetric variables of a portable X-band weather radar. The radome design introduces spatially dependent biases in polarimetric variables due to preferential loss of power in vertical polarization caused by metallic thread alignment. Due to the stochastic nature of radar measurements, these spatial errors exhibit variability across different scans. This study proposes a novel adaptive DFT algorithm to address the changing bias. The algorithm is formulated with the understanding that the bias caused by the radome joints remains constant along the range. Consequently, the DFT applied along the range exhibits an increase in magnitude in the zeroth frequency component (DC) for azimuth angles aligned with the radome joint positions compared to those misaligned. This leads to varying offset values of polarimetric variables across azimuths and elevations depending on the radar beam position with respect to radome joint positions. The algorithm detects and reduces the spatial bias pattern by suppressing the increase in offset values.

The algorithm's performance in mitigating the positive spatial bias in ZDR and PHIDP is evaluated by applying the algorithm in the PPI and RHI polarimetric variable scans measured during the Batsirai cyclone event on 3 February 2022. The results show that the adaptive DFT algorithm presented herein effectively addresses the spatial biases, enhancing the accuracy of ZDR and PHIDP measurements regardless of the scan type.

As the primary source of spatial bias originates from vertical polarization, the algorithm's effectiveness is further validated by examining the relationship between ZH and ZDR values. Notably, the correction reduces the positive bias observed in ZDR at lower reflectivity levels, bringing the mean ZDR value closer to the expected levels. Additionally, the algorithm reveals negative ZDR values, indicating the presence of attenuation fingerprints.

The proposed algorithm has limitations related to sample size and precipitation type. To effectively distinguish between meteorological targets and bias, it requires a large, noise-free sample along the range direction. Additionally, its performance relies on suppressing variations in the magnitude of the DC component of DFT observed across continuous azimuth angles. As a result, the algorithm performs optimally in scenarios characterized by uniform precipitation, such as stratiform precipitation and large convective systems that cover extensive areas around the radar. However, for isolated or scattered precipitation systems located in limited range and azimuth gates, the algorithm's performance needs to improve due to its inability to capture variations in the DC component magnitude derived from the DFT. To advance future research and potential improvements, an area of interest lies in evaluating the proposed algorithm's performance by conducting measurements both with and without the radome. An additional consideration is the possibility of incorporating a seamless monoblock radome as a future plan.

Data availability

All radar data is available at https://geosur.osureunion.fr/thredds/catalog/researchprogram/espoirs/1-Saint_Joseph/RADAR/Data/az-vol-75-0125-1to25deg-2022-01/2022/02/catalog.html. For information on rain gauge data, please send requests to ambinintsoa.ramanamahefa@univ-reunion.fr or visit the Météo France website https://portail-api.meteofrance.fr/web/fr/api/DonneesPubliquesObservation

Code avalaibility

The code is available upon request from the authors

Author Contributions

221 Thiruvengadam PADMANABHAN developed the algorithm, implemented the data analysis and wrote the paper, Guillaume
222 LESAGE and Ambinintsoa Volatiana RAMANAMAHEFA contributed to the implementation of the methodology and revised the
223 paper, Joël VAN BAELEN revised the paper and led the ESPOIRS project and radar field deployments.

Competing interests

225 The authors declare that they have no conflict of interest.

Acknowledgment

227 This work is part of the INTERREG V ESPOIRS project (Study of Precipitating Systems in the Indian Ocean by Radar and
228 Satellites). The ESPOIRS scientific program is led by LACy (University of La Réunion / CNRS / MétéoFrance) and funded by the
229 European Union (FEDER program - GURDTI/20201589-0021087), the Réunion Region, SGAR-Réunion, the French State (
230 CPER) and the University of La Réunion.

231
232

233
234

(a)   (b)   (c)

(d)
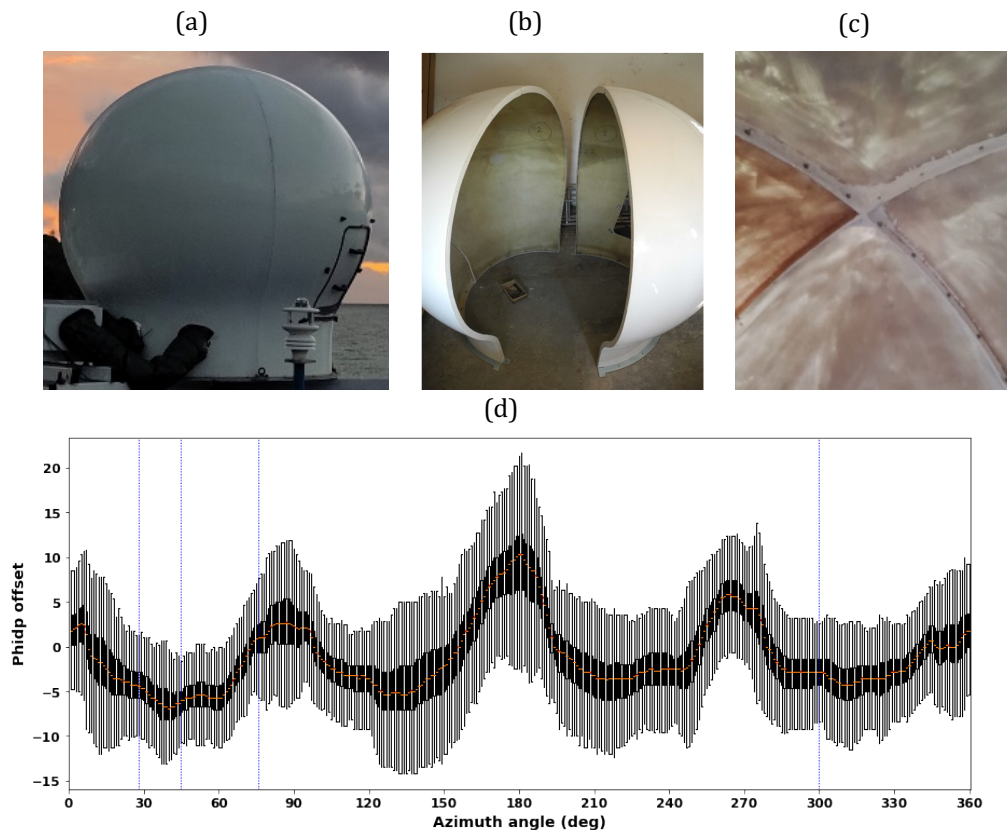
237 **Fig. 1.** Photographs illustrating the structure and assembly of the four lateral panels of the ESPOIRS Radar radome showing the regions of
238 metal nuts and bolts (a), (b), (c). Distribution of PHIDP offset obtained from all the PPI scans observed on 3rd February 2022 (d); the red dotted
239 line shows the median PHIDP offset. In the boxplot, black marks the interquartile range (25th to 75th percentiles), and grey whiskers extend 1.5
240 times the interquartile range. The blue dotted line indicates the azimuth location of RHI scans in fig 2.
241

242
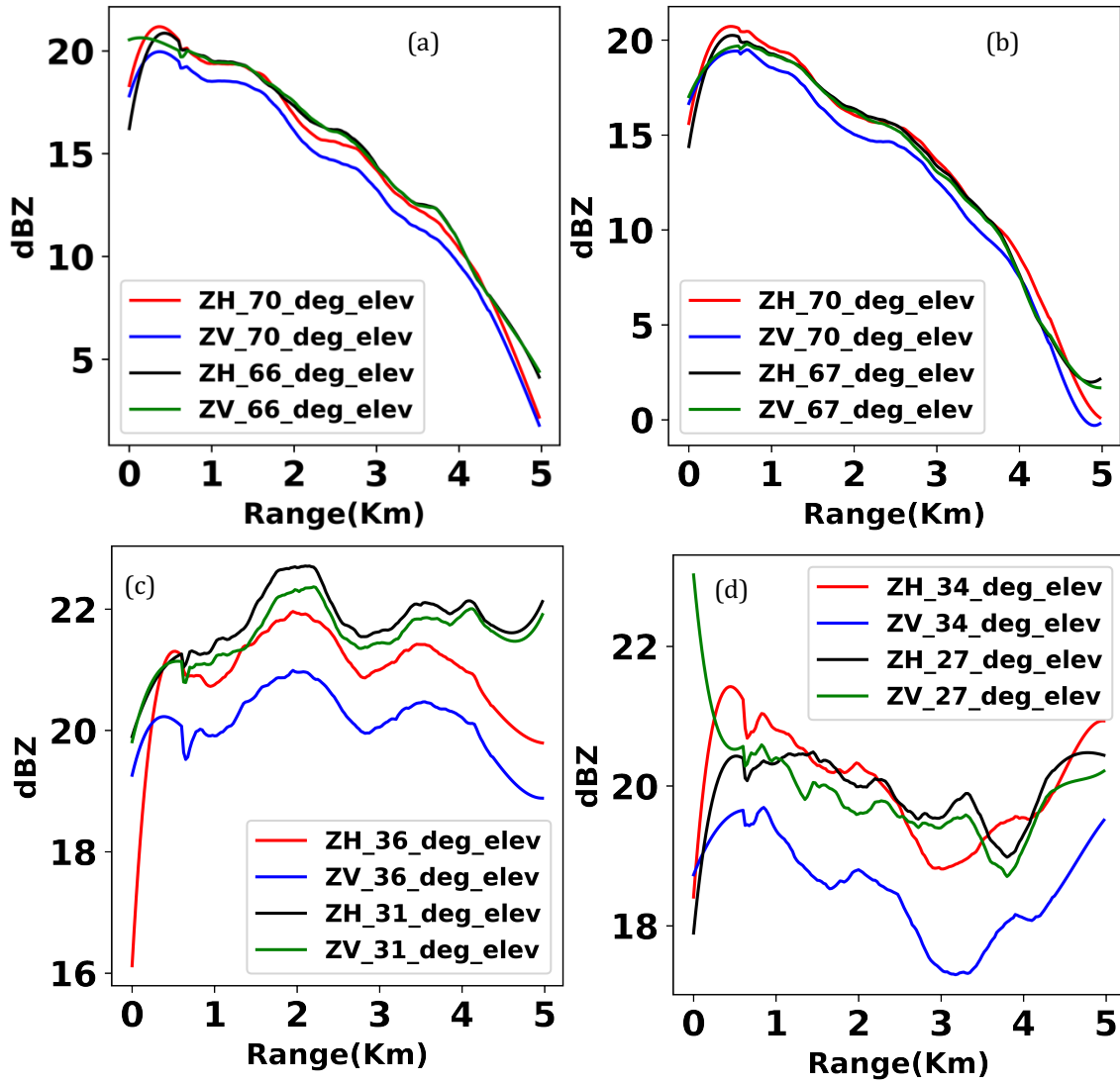
243
244
245 **Fig. 2.** The temporal median of horizontal and vertical reflectivity was obtained from RHI scan angles of (a) 28°, (b) 300°, (c) 45°, and (d)
246 76°, with corresponding elevation angles showing positive ZDR bias in red and blue (70°, 36°, and 34°) and unbiased elevation angles in green
247 and black (66°, 67°, 31°, and 27°) on February 3rd, 2022.
248
249
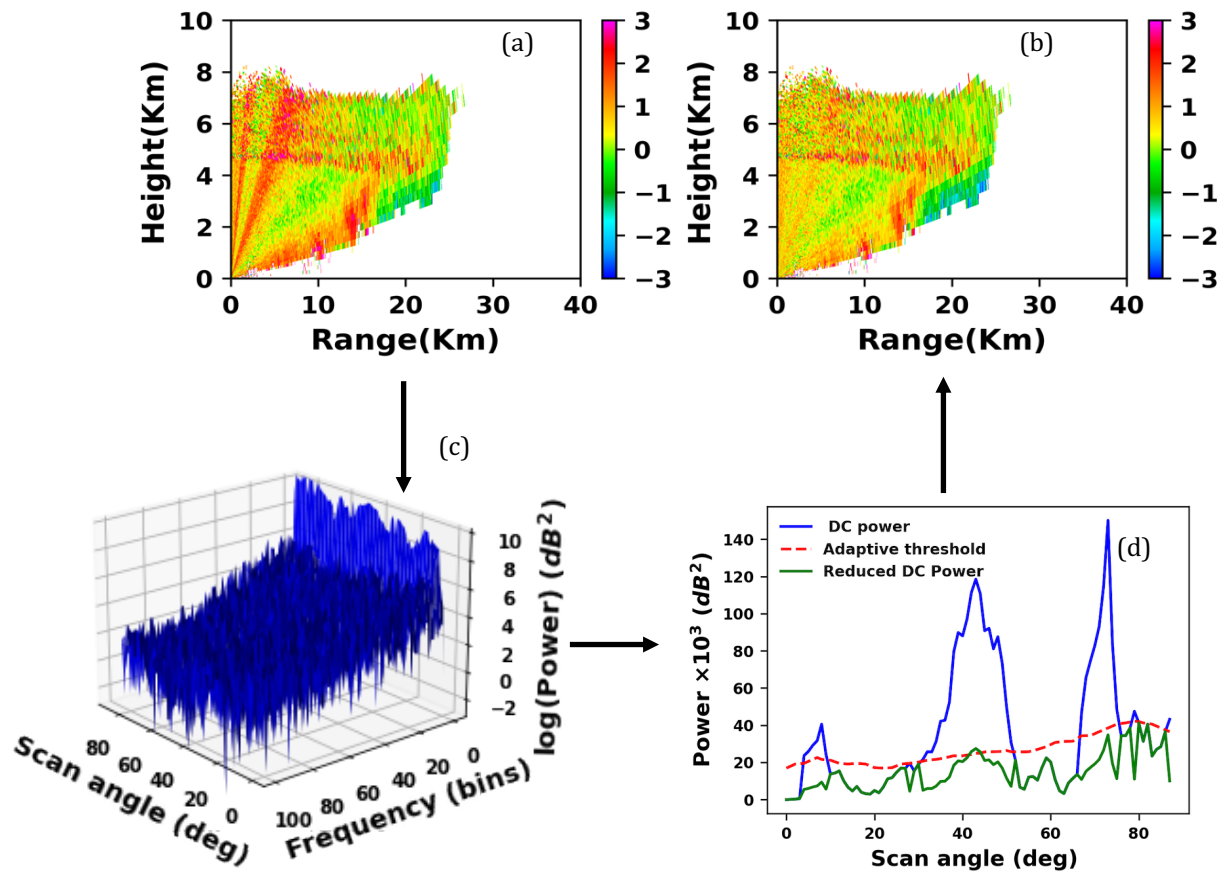
250
251
252 **Fig. 3**. 76° RHI scan of ZDR measured on 3rd February 2022 01:08 UTC before and after correction (a,b), 3D power spectrogram (c), The
253 power from zeroth frequency (DC) component (blue), adaptive threshold values (dotted red) and the reduced zeroth frequency power after the
254 application of the correction factor (d).
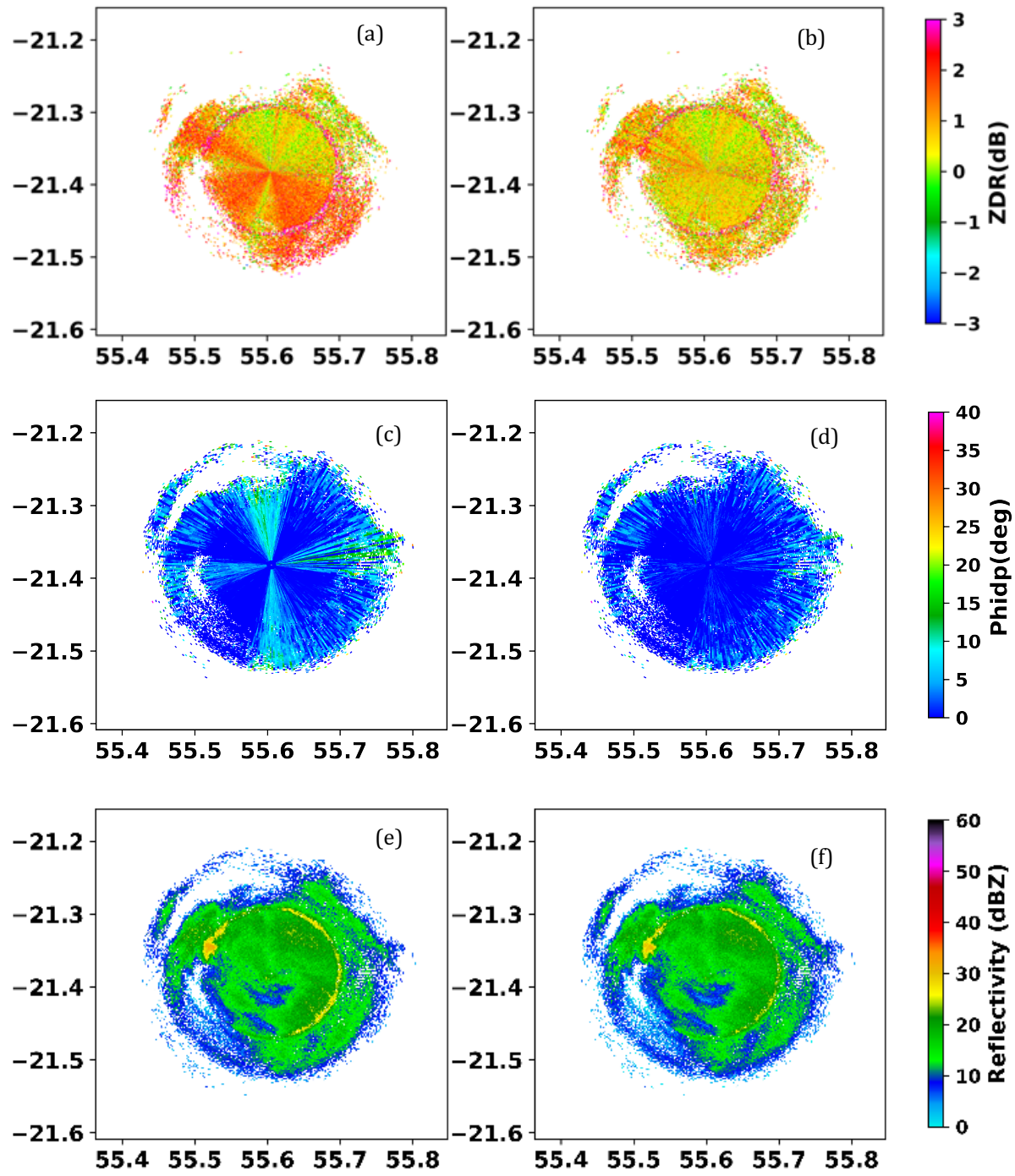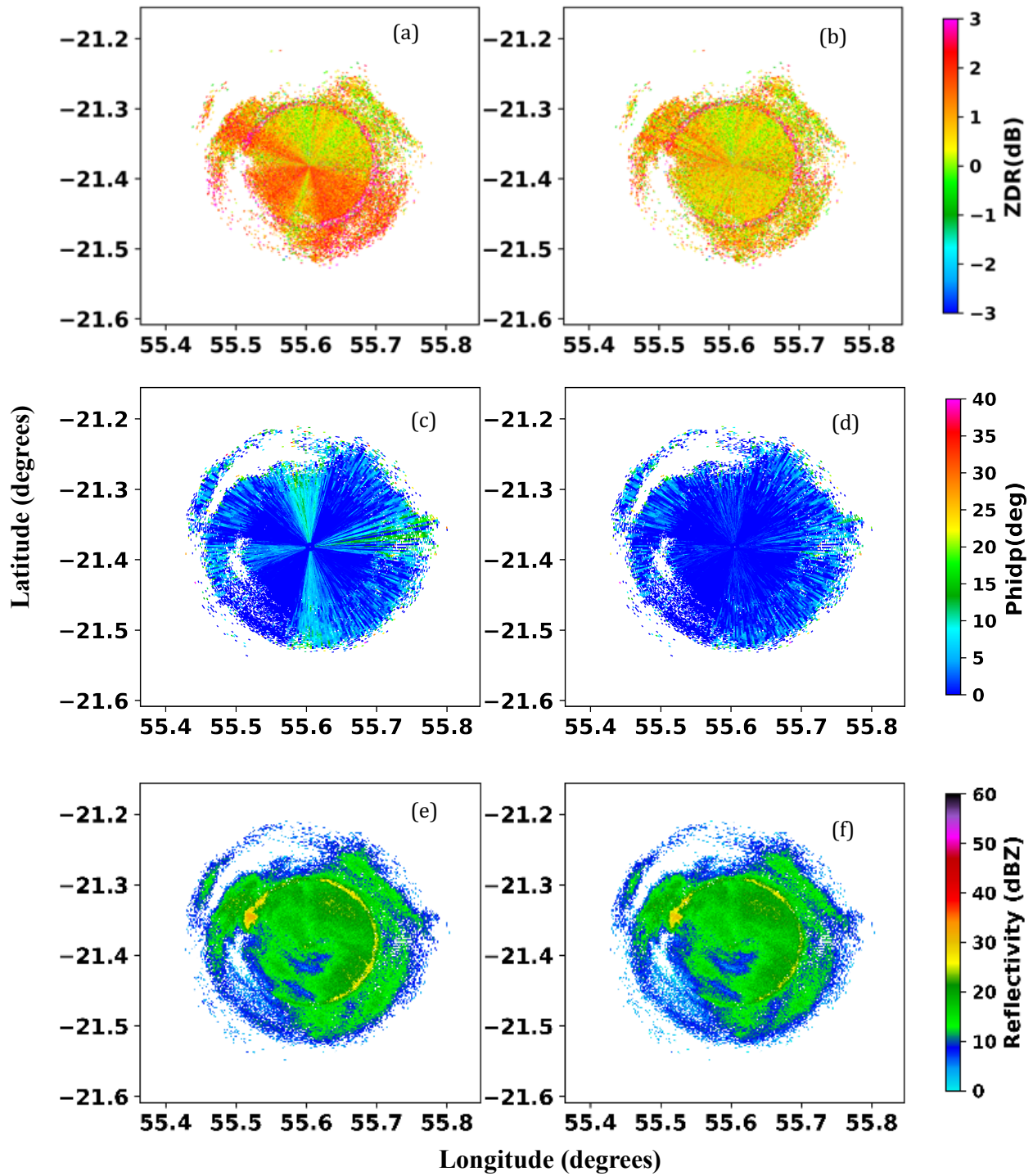
256
257   **Fig. 4.** 29° PPI scan of ZDR, PHIDP before correction (a, c) and after correction (b, d), horizontal (e) and vertical reflectivity (f) measured on
258   03 February 2022 01:50 UTC.
259

(a)   (b)   (c)
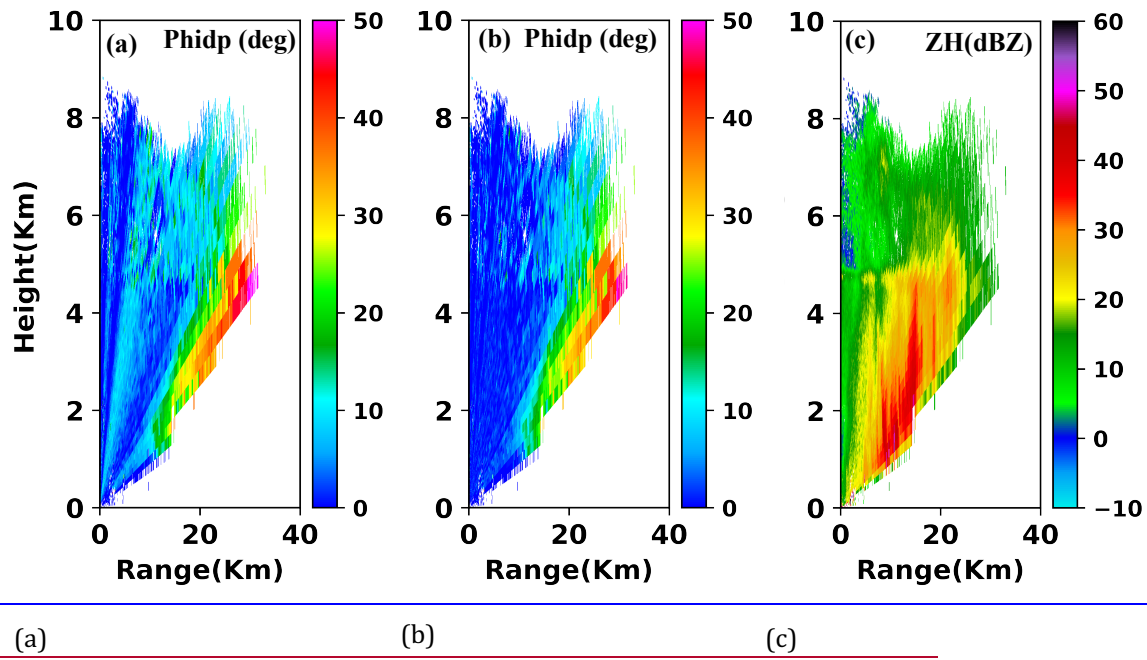
Fig. 5. 28° RHI scan of PHIDP before and after correction (a, b) along with ZH (c) on 03 February 2022 01:28 UTC.
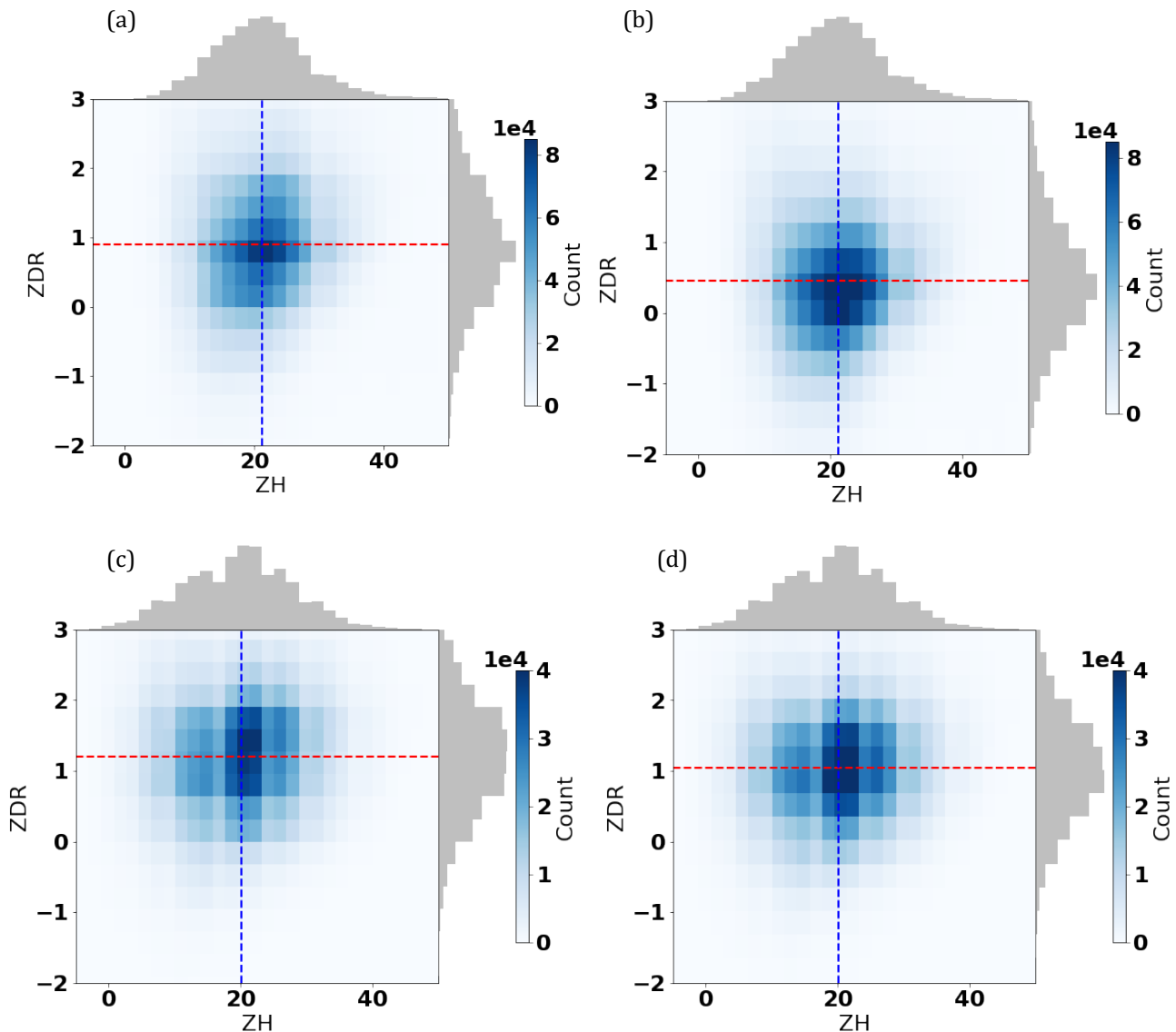
Fig. 6. Joint histograms of ZDR and ZH for (a) PPI scans before and (b) after correction, as well as (c) RHI scans before and (d) after correction, all from scans conducted on February 3, 2002, with the marginal distribution of ZH in the top and the marginal distribution of ZDR on the right side. The red dotted line represents the median of ZDR, while the blue dotted line represents the median of ZH.

References

Figueras i Ventura, J., Boumahmoud, A. A., Fradon, B., Dupuy, P., and Tabary, P.: Long-term monitoring of French polarimetric radar data quality and evaluation of several polarimetric quantitative precipitation estimators in ideal conditions for operational implementation at C-band, Quarterly Journal of the Royal Meteorological Society, 138, https://doi.org/10.1002/qj.1934, 2012.

Figueras i Ventura, J., Schauwecker, Z., Lainer, M., and Grazioli, J.: On the Effect of Radome Characteristics on Polarimetric Moments and Sun Measurements of a Weather Radar, IEEE Geoscience and Remote Sensing Letters, 18, 642–646, https://doi.org/10.1109/LGRS.2020.2981993, 2021.

Frech, M., Lange, B., Mammen, T., Seltmann, J., Morehead, C., and Rowan, J.: Influence of a radome on antenna performance, J Atmos Ocean Technol, 30, https://doi.org/10.1175/JTECH-D-12-00033.1, 2013.

Georgis, J. F., Roux, F., and Hildebrand, P. H.: Observation of Precipitating Systems over Complex Orography with Meteorological Doppler Radars: A Feasibility Study, Meteorology and Atmospheric Physics, 72, 185–202, https://doi.org/10.1007/s007030050015, 2000.

Gourley, J. J., Tabary, P., and du Chatelet, J. P.: Data Quality of the Meteo-France C-Band Polarimetric Radar, J Atmos Ocean Technol, 23, 1340–1356, https://doi.org/https://doi.org/10.1175/JTECH1912.1, 2006.

286 Li, P., Li, N., Xu, W., and Song, L.: Phase Compensation of Composite Material Radomes Based on the Radiation Pattern,
287 Chinese Journal of Mechanical Engineering (English Edition), 30, https://doi.org/10.1007/s10033-017-0133-1, 2017.
288 Mishra, S., Sarkar, M., and Daniel, A.: Optimization of radome wall and joint for X-band reflector antenna using Floquet
289 modal analysis, J Electromagn Waves Appl, 28, 1257–1268, https://doi.org/10.1080/09205071.2014.914859, 2014.
290 Park, S.-G., Bringi, V. N., Chandrasekar, V., Maki, M., and Iwanami, K.: Correction of Radar Reflectivity and Differential
291 Reflectivity for Rain Attenuation at X Band. Part I: Theoretical and Empirical Basis, J Atmos Ocean Technol, 22, 1621–1632,
292 https://doi.org/https://doi.org/10.1175/JTECH1803.1, 2005.
293 Ryzhkov, A. V, Zhuravlyov, V. B., and Rybakova, N. A.: Preliminary Results of X-Band Polarization Radar Studies of
294 Clouds and Precipitation, J Atmos Ocean Technol, 11, 132–139, https://doi.org/https://doi.org/10.1175/1520-
295 0426(1994)011<0132:PROXBP>2.0.CO;2, 1994.
296
297